Electrochimica Acta 166 (2015) 1–11

Contents lists available at ScienceDirect

Electrochimica Acta

journal homepage: www.elsevier.com/locate/electacta

Promising biomass-based activated carbons derived from willow catkins for high performance supercapacitors

Kai Wang [a,b], Ning Zhao [a], Shiwen Lei [a], Rui Yan [a,b], Xiaodong Tian [a,b], Junzhong Wang [a], Yan Song [a,*], Defang Xu [a,b], Quangui Guo [a], Lang Liu [a]

[a] Key Laboratory of Carbon Materials, Institute of Coal Chemistry, Chinese Academy of Sciences, 27 South Taoyuan Road, Taiyuan 030001, PR China
[b] University of Chinese Academy of Sciences, Beijing 100049, PR China

ARTICLE INFO

Article history:
Received 1 December 2014
Received in revised form 16 February 2015
Accepted 8 March 2015
Available online 10 March 2015

Key words:
Willow catkins
Activated carbon
Waste biomass
Supercapacitor
Potassium hydroxide activation

ABSTRACT

Unusual sheets-like primary activated carbon particles interconnected into three-dimensional micrometer-level large pores were prepared from a novel biomass named willow catkins (WCs) by KOH chemical activation process and used as electrode materials for supercapacitors. The pore structures, surface area and chemical properties could be facilely adjusted by changing the activation temperature. When the activation temperature increased from 600 to 800 °C, the specific surface area of the porous carbon product increased remarkably while the contents of nitrogen and oxygen co-doped decreased, which significantly affected the electrochemical properties of the porous carbon-based supercapacitors. The activated carbons from 600 °C activation possesses despite moderate specific surface area (645 $m^2 g^{-1}$), concentrated pore size distribution of 0.77 nm, but high nitrogen (2.51 wt.%) and oxygen (13.28 wt.%) contents, high graphitization degree as well as good electrical conductivity. The supercapacitors with the carbon electrode reached maximal specific capacitances of 340 $F g^{-1}$ and high specific surface capacitance of 52.7 $\mu F cm^{-2}$ at the current density of 0.1 $A g^{-1}$, good rate capability (231 $F g^{-1}$ at 10 $A g^{-1}$) and good cycling stability (92% capacitance retention over 3000 cycles). The favorable capacitive performances make the waste biomass WCs act as a new resource of carbonaceous materials for high performance supercapacitors.

1. Introduction

Supercapacitors, also known as electrochemical capacitors or ultracapacitors, have attracted more and more attention due to the advantages of high power density, long cycle life (>100 000 cycles), rapid charging–discharging rate, simple principles and fast dynamics of charge propagation [1–3]. As a result, supercapacitors are widely used in consumer electronics, electric vehicles, pulsing techniques as well as industrial power and energy management [4,5]. A more recent application for supercapacitors in emergency doors on the Airbus A380 highlights their security and reliability. Generally, on the basis of the energy storage mechanism, supercapacitors can be classified into two categories: electrical double layer capacitor (EDLC) and pseudo-capacitor [6–8]. The capacitance for EDLC comes from the pure electrostatic charge accumulation at the electrode/electrolyte interface, which is greatly dependent on the surface area of the electrode materials that is accessible to electrolyte ions. The pseudo-capacitor is related with the fast and reversible faradic process of the electroactive species within the electrode materials. For pseudo-capacitive materials, mainly metal oxides and electrical conductive polymers, have been widely used as high specific capacitance electrode. However, low conductivity, poor cycle stability as well as high cost that greatly limited its practical application as electrode materials.

Porous carbonaceous materials with tunable porosities, including activated carbons (ACs) [7,9], ordered mesoporous carbons [10], carbon aerogels [11,12] and graphene-based materials [13], have been extensively used as electrode materials in the commerical supercapacitors. Among these carbon materials, ACs is considered as one of the most attractive candidates for supercapacitors due to its high specific surface area, well-developed porous structure, high electrical conductivity and electrochemical stability. Traditionally, the preparation of ACs mainly involves the coal, petroleum and their derivatives that are expensive and non-renewable. Considering the potentially scalable and sustainable of supercapacitor applications, the development of low-cost carbon materials from renewable raw materials is very worthwhile. Biomass materials, benefiting from the renewable, low-cost and eco-friendly properties as compared

* Corresponding author. Tel.: +86 351 2021135; fax: +86 351 2021135.
E-mail address: yansong1026@126.com (Y. Song).

http://dx.doi.org/10.1016/j.electacta.2015.03.048
0013-4686/

to the non-renewable and diminishing fossil resources [14,15], are rich sources of carbon but may also contain other elements such as oxygen, nitrogen and so on. Usually direct burning of the biomass materials will lead to environmental pollution because of the emission of the CO_2 and/or nitrogen oxides (NO_x) into the atmospheres. Therefore, how to make use of these plentiful waste biomasses efficiently has greatly attracted researchers' attention. Up to now, a wide variety of waste biomass materials, including celtuce leaves [16], tea leaves [17], dead neem leaves [18], corn grains [19], sunflower seed shell [20], pistachio and firwood [21,22], coconut shell [23,24], rice husk [25], bamboo [26], entermorpha prolifera [27], seaweed [2], fermented rice [28], waste newspaper [29], bacteria [6], fungi [30], animal's bones [31,32] and animal's feather [33], etc., have been utilized as carbon precursors to prepare porous carbonaceous materials that have shown great potential as electrode materials for supercapacitors.

Willow, which belongs to genus Salix of deciduous trees, has widely distributed in cold and temperate regions of the Northern Hemisphere. Catkins are willow flowers appearing on the branches, produced in the early spring before the leaves or as the new leaves open. Every spring innumerable white floccule floating in air, brings a lot of trouble for people, for examples, respiratory ailments or skin anaphylaxis. A reasonable and effective approach for overcoming this air pollution problem is very limited. In this regard, a practical and feasible technique to solve this problem is to transform these waste biomasses to high value-added products rather than just burn them. Recently, Ma and co-workers used willow catkins (WCs) as precursors to prepare carbon microtubes by simple carbonization and the carbonaceous materials exhibit good activity in the oxygen reduction reaction [34].The specific hollow tubular-liked structure or morphology and rich heteroatoms compositions of WCs would lead to the generation of carbonaceous materials with specific pore structure or morphology and chemical properties. Herein, the aim of our research work is to exploit a new way for biomass waste application, which could not only solve the problems of biomass pollution but also enrich the choice of precursors for electrode materials.

In this study, willow catkins were used as the precursor to synthesize unusual porous activated carbons by simple KOH activation process for the first time. The activated carbon products have three-dimensional large pores at micrometer size and narrow micropores of 0.77–1.2 nm and are significantly doped by nitrogen/oxygen. The AC products can be milled and sonicated to make a colloidal dispersion that is convenient to make a uniform film. We found that the specific surface area of ACs increased but surface heteroatoms contents decreased when the activation temperature increased from 600 °C to 800 °C. The relationship between the structure characteristics, surface chemical properties of the porous carbon and its electrochemical performance are investigated intensively. Interestingly, electrochemical performances of the ACs based supercapacitors depends more on heteroatoms contents than the specific surface area of the ACs. The sample obtained at 600 °C despite have moderate specific surface area, controllable pore size distribution and rich suface nitrogen- and oxygen-containing functional groups, high graphitization degree as well as good electrical conductivity that resulting in higher specific capacitance than those obtained at 700 °C and 800 °C. The results further demonstrated that the as-prepared ACs is a promising electrode material in energy storage application.

2. Experiments

2.1. Preparation of WCs derived ACs

WCs were collected in large quantity from Taiyuan city, Shanxi province between March and April. As a facile and scalable synthesis method, the porous ACs from WCs were prepared as follows. First, a certain amount of WCs was washed with deionized water for several times to remove adherent soil and impurities. Then, it was dried at 120 °C for 12 h. The dried WCs were fully stirred in aqueous KOH solution (the mass ratio of KOH to WCs equals to 1(g/g)) for 1 h at room temperature and followed by evaporating water at 80 °C under vacuum and dried at 120 °C overnight. The dried sample was pyrolyzed in a nickel crucible at 600–800 °C for 1 h with a heating rate of 5 °C min^{-1} under a nitrogen flow (30 ml min^{-1}). Then, the resulting solid was repeatedly washed with 1 M HCl and deionized water until the pH value of filtrate reached to about 7. The residue was dried at 90 °C for 5 h. The resultant porous ACs were denoted as AC-*T*, where *T* was corresponding to the heat treatment temperature.

2.2. Characterization of Samples

The thermogravimetric (TG) and derivative thermogravimetric (DTG) analyses were carried out on a NETZSCH STA 409 PC/PG thermal analysis instrument at a heating rate of 10 °C min^{-1} in N_2 atmosphere. Field emission scanning electron microscopy (FESEM) images were performed on a JEOL JSM-7001F microscope at an accelerating voltage of 10 kV. The TEM images were taken on FEI Tecnai G2 F20 S-twin transmission electron microscope with an acceleration voltage of 100 kV. Powder X-ray diffraction (XRD) patterns were examined on a D8 ADVANCE diffractometer with CuKα radiation (λ = 1.5418 Å) operating at 40 kV, 15 mA. The Raman spectra were recorded on a Horiba (XploRA) spectrometer. The source of radiation was a laser operating at a wavelength of 514 nm and power of 25 mW. X-ray photoelectron spectra (XPS) were measured on a Kratos AXIS Ultra DLD spectrometer with Al target, Kα radiation, from a double anode X-ray source. Nitrogen sorption isotherms and physical properties were examined by ASAP 2020 physisorption apparatus at 77 K. The samples were degassed at 250 °C for 5 h prior to the measurement. The surface area was calculated by the Brunauer–Emmett–Teller (BET) method based on the nitrogen adsorption data in the P/P_o range corresponding to the linear region. The total pore volume was estimated with the amount of nitrogen adsorbed at a relative pressure of $P/P_o = 0.99$. The pore size distribution (PSD) was obtained by the non-local density functional theory (NLDFT) method with an assumption of slit pore model. The Fourier transformation infrared (FT-IR) spectra in the region from 400 to 4000 cm^{-1} were recorded on a Bruker VERTEX 70 spectrometer by using KBr pellet technique. The element contents in the feed and carbonaceous materials were measured by Vario EL Cube elemental analyzer.

2.3. Electrochemical Measurements

Three-electrode configuration was adopted to evaluate the capacitive performance of the as-prepared activated materials on a CHI 660C electrochemical workstation (Shanghai ChenHua Instruments Co., China). The test was performed in 6 M KOH aqueous electrolyte solution under ambient conditions. A platinum foil and saturated calomel electrode (SCE) were used as the counter electrode and reference electrode, respectively. The working electrodes were prepared by mixing the activated materials, acetylene black, conducting graphite, and polytetrafluoroethylene (PTFE) binder at a weight ratio of 75:10:10:5. A small amount of ethanol was added and the mixture was pestled by mortar to form an evenly slurry. The slurry was coated onto a nickel foam current collector and dried at 60 °C overnight in a vacuum. The capacitive performance of samples were studied by using cyclic voltammetry (CV), galvanostatic charge–discharge (GCD) and electrochemical impedance spectroscopy (EIS) techniques. The working voltage windows were between −0.9 and 0 V. EIS was performed in a

frequency range of 10 mHz to100 kHz at the open circuit voltage with alternate current amplitude of 5 mV. The specific capacitance of the three-electrode system was calculated by using the following formula:

$$C = \frac{I\Delta t}{m\Delta V} \tag{1}$$

where C is the specific capacitance ($F\,g^{-1}$), I is the discharge current (A), Δt is the discharge time (s), m represents the mass of active material in the electrode (g) and ΔV is the potential change in discharge (V).

From the EIS data, the specific capacitance of the activated carbon was calculated using the following equation:

$$C = -\frac{1}{2\pi f Z'' m} \tag{2}$$

where f is frequency (Hz), and Z'' is imaginary impedance at f.

The EIS data as a function of the frequency were analyzed using the following equations:

$$Z(\omega) = \frac{1}{j\omega C(\omega)} \tag{3}$$

$$Z(\omega) = Z'(\omega) + jZ''(\omega) \tag{4}$$

$$C(\omega) = C'(\omega) - jC''(\omega) \tag{5}$$

$$C'(\omega) = -\frac{Z''(\omega)}{\omega|Z(\omega)|^2} \tag{6}$$

$$C''(\omega) = -\frac{Z'(\omega)}{\omega|Z(\omega)|^2} \tag{7}$$

$$\tau_0 = \frac{1}{2\omega} = \frac{1}{2\pi f_0} \tag{8}$$

where $Z(\omega)$ is complex impedance, $Z'(\omega)$ is real impedance, $Z''(\omega)$ is imaginary impedance, $C(\omega)$ is complex specific capacitance ($F\,g^{-1}$), $C'(\omega)$ is real capacitance, $C''(\omega)$ is imaginary capacitance, f_0 is a frequency corresponding to peak capacitance of $C''(\omega)$, and τ_0 is time relaxation constant.

3. Results and discussion

The biomass willow catkins exhibit fluffy and lightweight macroscopic appearance (Fig. 1a) and can fly everywhere. The special characteristics make the as-prepared activated carbon show low apparent density (inset in Fig. 2a) and well-developed pore structure. The SEM images show that the WCs are acturally hollow micro-tubes. As shown in Fig. 1b and c, the microtubular strctures have the diameter of 7∼17 μm and the tube wall thickness is around 1 μm. They look like hollow fibers, but have a higher hollowness [35,36]. Fig. 1d presents the thermal decomposition behavior of the WCs in a N_2 flow (30 ml min^{-1}). The precursor weight loss as a function of pyrolysis temperature is measured from the thermogravimetric curves. The pyrolysis of WCs can be attributed to the pyrolysis of hemicellulose, cellulose, and lignin. It can be seen that the weight loss mainly occurred between 200 °C and 600 °C with three stages. The broad peak at 77 °C in the DTG curve is attributed to the removal of physically adsorbed water and the dehydration of WCs, while another sharp

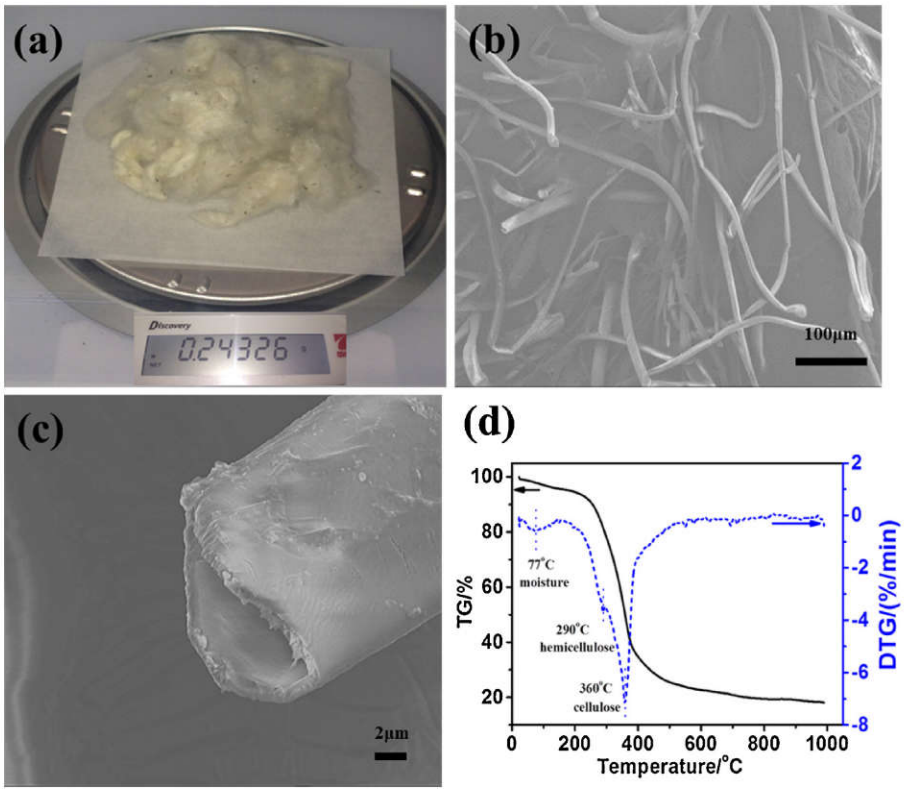

Fig. 1. Optical photograph of the biomass willow catkins (WCs) (a); SEM images of the WCs (b,c); TG/DTG curves of WCs measured at a heating rate of 10 °C min^{-1} in N_2 atmosphere (d).

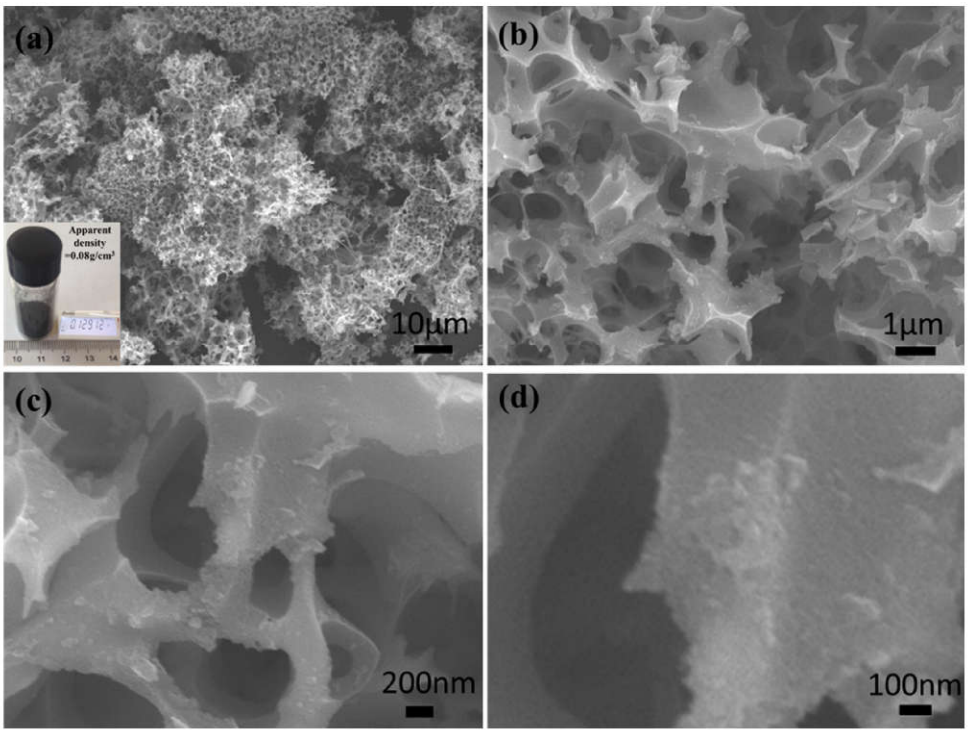

Fig. 2. SEM images of the activated carbon products obtained at 600 °C with different magnifications (a–d); the inset in Fig. 2a is the photograph of the powder product sample.

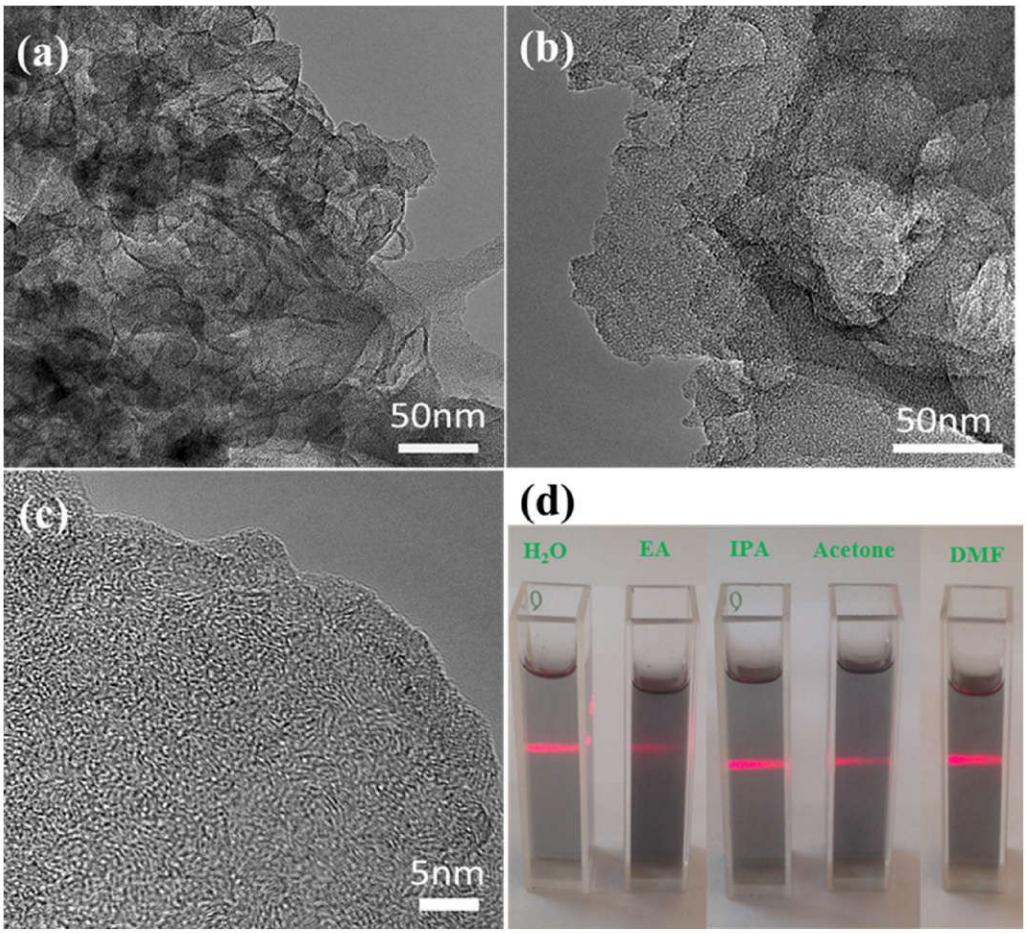

Fig. 3. TEM images of the activated carbons obtained at 600 °C with different magnifications (a–c); Photographs of colloidal ACs in various solvents with a red laser line irradiated (d) (For interpretation of the references to color in this figure legend, the reader is referred to the web version of this article.).

peak at 360 °C with a shoulder peak at around 290 °C is attributed to the thermal decomposition of cellulose and hemicellulose, respectively [37]. The TG curve tends to flatten owing to the pyrolysis of lignin at higher temperature [38]. It is well-known that the decomposition of lignin is over a wide temperature range with no distinguishable peak [39]. In general, the weight losses of WCs at the range of 200–600 °C are larger than those over 600 °C because the lignin is more inclined to form char than hemicelluloses and cellulose. The result also indicates that the pyrolysis behavior of WCs is similar to that of lignocellulosic biomass [23,40].

The WCs were activated at the temperatures ranging from 600 °C to 800 °C at N_2 atmosphere. The AC products were clearly observed by electron microscopes (Fig. 2 and Fig. S1). As shown in Fig. 2, SEM images present the ACs are three-dimensional porous network structure with micrometer-level large pores. When the walls of large pores were closely observed, the walls look like particular with a number of <100 nm particles connected (Fig. 2d). TEM images give the evidences that the particles are sheets-like, as presented in Fig. 3a,b. High resolution TEM shows that a sheet has rich micropores of around 1 nm (Fig. 3c). Very interestingly, the powder with the sheets-like microstructure can be readily milled and sonicated to make a colloidal dispersions in vary solvents (Fig. 3d). The colloidal dispersion is convenient to prepare uniform films, which is advantageous for many hard AC products from wood biomasses.

The XRD patterns of the feed WCs and as-prepared activated samples obtained at different temperature are shown in Fig. 4a. For the WCs, the diffraction peak at about 21.7° is attributed to the cellulose, similar to that of cotton fiber or wheat straw [41,42]. The sharp peak at 26.7° indicates the existence of crystalline inorganic compounds ascribed to the trace elements within the WCs [16]. The intensity of this peak becomes lower when increasing of the activation temperature, and almost disappears at 800 °C owning to the reducing of the trace elements. The broad and low intensity peaks for the activated samples are observed at around 23.4° and 43.9°, which correspond to the diffraction of (0 0 2) and (1 0 0) plane of the graphite lattice, respectively, although disordered [43]. With increasing of the activation temperature, the two peaks become broader and the intensity decreases, especially for the diffraction of (1 0 0) plane that disappears over 700 °C which demonstrates that the order degree of graphitization of samples decrease at higher activation temperature [44]. Moreover, the graphitic structure of activated samples are characterized by Raman spectra (Fig. 4b). All the samples mainly show two distinct peaks located at around 1353 (D-band) and 1581 cm^{-1} (G-band), which are attributed to defected carbon crystallites and crystalline graphite, respectively [45,46]. The D-band is assigned to the breathing mode of κ-point phonons of A_{1g} symmetry for the disordered graphite. While the G-band corresponds to E_{2g} mode of 2D graphite, which is related to the vibration of sp^2-hybridized carbon atoms in a two-dimensional hexagonal lattice [24]. The relative intensity of D-band and G-band (I_D/I_G) is proportional to the crystalline degree of carbon materials. The I_D/I_G values of AC-600, AC-700, and AC-800 are determined to be 0.79, 0.82 and 0.84, respectively. As the activation temperature increased from 600 to 800 °C, the I_D/I_G value increased, suggesting the highest graphitization degree of AC-600. These results are in good accordance with the XRD analysis presented in Fig. 4a.

The evolution of the chemical compositions of the feed WCs and the activated samples obtained at different activation temperature are characterized by Fourier-transform infrared (FT-IR) spectroscopy. As shown in Fig. 5a, with increasing of the activation temperature, the bands become broader and weaker due to the strong absorption of the carbon materials. The broad peak at 3420 cm^{-1} can be assigned to the N—H symmetric stretching vibration and/or hydrogen-bonded hydroxyl [47]. The bands at 2925 and 2854 cm^{-1} are due to the C—H stretching vibrations [48], and the bands at 1460 and 1385 cm^{-1} are ascribed to the C—H deformation vibrations, while the band at 1740 cm^{-1} is attributed to the C=O stretching vibrations. The peak at around 1604 cm^{-1} is correspond to N=H in-plane deformation vibrations and/or C=C stretching vibration, which reflects the existence of aromatic rings or both species. The broad peak at around 1246 cm^{-1} is assigned to the C—N stretching vibration [42]. The band at 1162 cm^{-1} may be assigned to C—O vibrations in phenols, ethers, or esters [49]. Hence, the FT-IR analysis indicates the existence of nitrogen and oxygen species in the as-prepared porous ACs.

In addition, X-ray photoelectron spectroscopy (XPS) measurement further confirms the weak signal at the binding energy of 400 eV for N 1s spectra and pronounced signal at 532 eV for O 1s (Fig. 5b). As listed in Table 1, the porous ACs are rich in surface active nitrogen- and oxygen-containing functional groups. The N 1s region spectrum can be deconvoluted to three peaks, which are

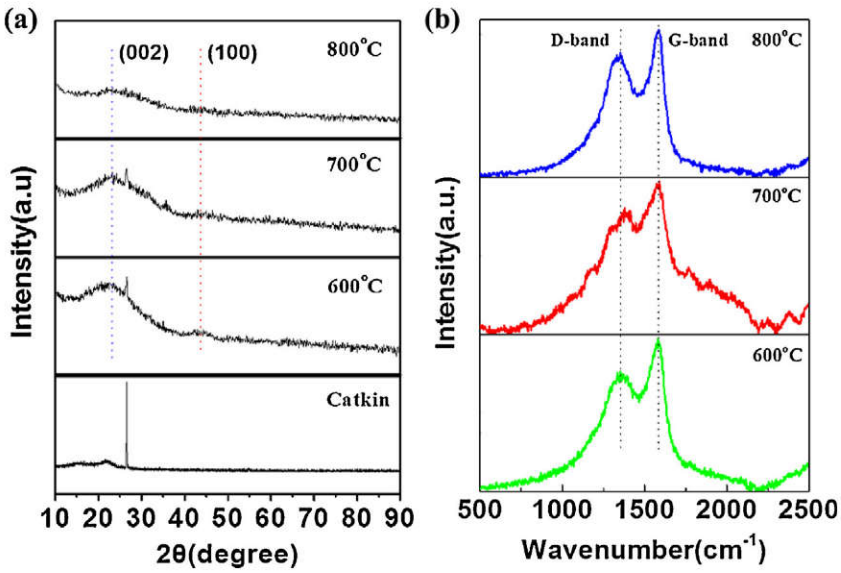

Fig. 4. (a) XRD curves and (b) Raman spectra of WCs and their activated samples obtained at different temperatures.

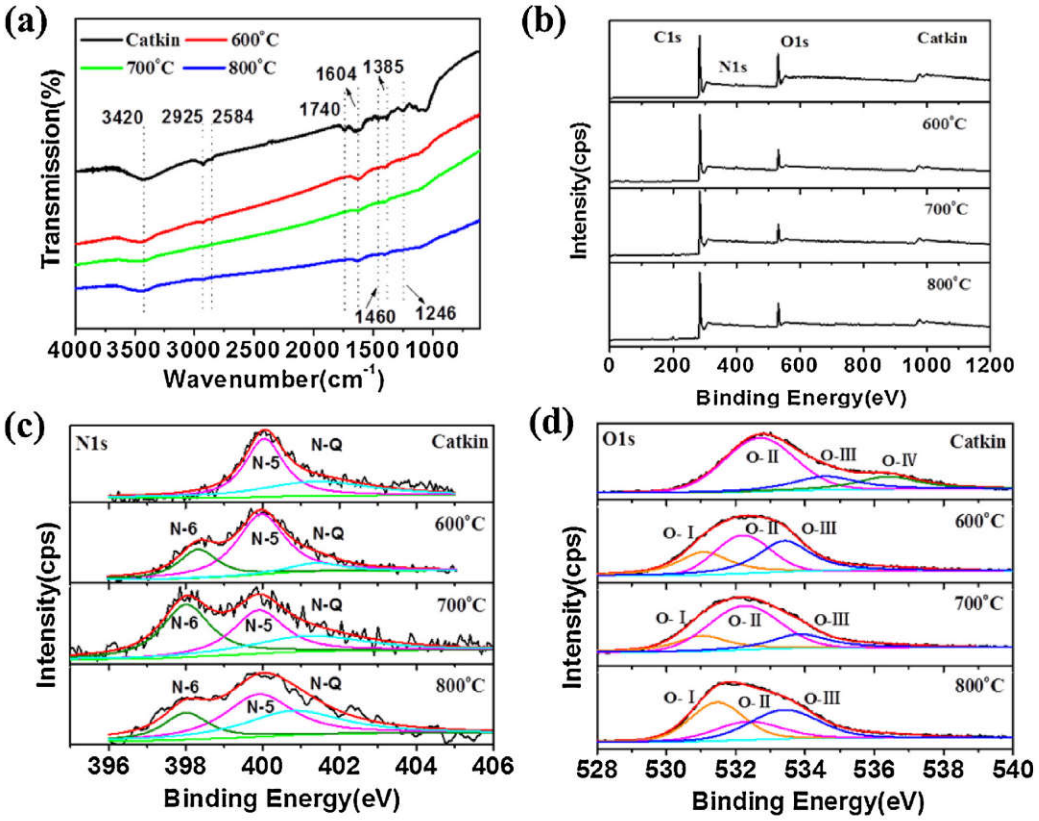

Fig. 5. (a) FT-IR spectra and (b) XPS survey spectra, High-resolution XPS spectra of (c) the deconvoluted N 1s peak and (d) O 1s peak.

Table 1
Chemical compositions and surface functional groups of the as-prepared ACs.

Sample	Elemental analysis (wt.%)				at.% of total N1s (by XPS)			at.% of total O1s (by XPS)		
	C	N	O	H	N-6	N-5	N-Q	O-I	O-II	O-III
WCs	47.22	2.17	39.55	6.18	0	77.8	22.2	-	62.9	19.6
AC-600	74.63	2.51	13.28	2.51	20.6	70.4	9.0	27.6	34.8	37.6
AC-700	80.82	1.39	9.95	1.38	38.8	34.1	27.1	21.4	58.2	20.4
AC-800	87.04	0.95	5.55	0.64	18.8	44.6	36.6	39.0	23.3	37.7

corresponding to three types of nitrogen functional group, namely pyridinic (N-6, 398.7 ± 0.3 eV), pyrrolic and/or pyridonic (N-5, 400.3 ± 0.3 eV) and quaternary nitrogen (N-Q, 401.4 ± 0.5 eV) [8]. N-6 is pyridinic N, that is, N bonds to two C atoms in six-membered rings at the edge of the graphene layer. N-5 represents pyrrolic N or pyridonic N in a five-membered ring that is associated with phenolic or carbonyl group on the neighbor carbon atoms of the ring. The N-Q is quaternary N, that is, N bonds to three C atoms and locates in the central or valley position of graphene layer. The nitrogen content and types have great effect on the capacitive performance for providing faradaic pseudo-capacitance. For the WCs, only the peaks at 400.1 and 401.5 eV corresponding to N-5 and N-Q, respectively, are observed. However, for the porous ACs, the peak of N-6 appears. The total nitrogen content decreases from 2.51 wt.% for AC-600 to 0.95 wt.% for AC-800 with increasing of the activation temperature (Table 1) and the N-5 content decrease when compare with the feed WCs because of the denitrogenation and aromatization. By increasing the activation temperature, the total amounts of N-6 and N-5 decrease gradually, while the N-Q content increases significantly. The porous ACs prepared at 600 °C have less amount of N-Q (9.0% of total nitrogen content) than the samples prepared at the 700 °C (27.1%) and 800 °C (36.6%). It suggests that the nitrogen species tend to form N-Q with relatively higher binding energy at higher activation temperature. The result is also confirmed by other reports [8,50]. It is reported that the most important functional groups affecting energy storage performance are pyrrolic and pyridnic nitrogen [51], while the nitrogen functionalities locating at the middle of graphite (N-Q) are found generally less active [52]. The results indicate that the high specific capacitor performance for AC-600 is partially due to the higher amounts of exposed N-6 and N-5 rather than N-Q species that provide the initial electrochemical active sites for pseudocapacitive interaction. Fig. 5d depicts the deconvolutions of O 1s region spectrum that identify the surface oxygen-containing functional groups. The binding energies corresponding to appropriate peaks are as follows: 531.3 ± 0.2 eV, carbonyl (C=O) and/or quinone (marked as O-I); 532.4 ± 0.3 eV, hydroxyl (C—OH) and ether (C—O—C) (marked as O-II); 533.9 ± 0.5 eV, carbonxyl (COO^-) (marked as O-III); 536.3 ± 0.2 eV, chemisorbed oxygen and/or water (marked as O-III). Based on the previous reports, O-I and O-II (basic oxygen groups), are credited with electrochemical redox activity, which are considered to contribute to pseudocapacitance [51]. In addition to the pseudocapacitance contribution, both the surface nitrogen- and oxygen-containing functional groups also play an important role in improving the hydrophilicity and

wettability of the material surface and facilitating the accessibility of the electrolyte ions.

Nitrogen adsorption-desorption isotherms of porous ACs prepared at different activation temperatures are shown in Fig. 6a. All the samples exhibit typical characteristics of Type-I isotherms with unapparent hysteresis loop (according to the IUPAC classification) [33]. The isotherms show a steep gas uptake at very low relative pressure and a fairly flat plateau in the high pressure that implies the porous ACs are predominantly microporous with small amounts of mesopores [53]. The activation temperature has a remarkable effect on the pore structure of ACs. As the KOH activation process deepened at higher temperature, more micropores were generated and the ultromicropores were widened, resulting in higher surface area and total pore volume (see Table 2). The PSD and pore volumes are determined by hybrid NLDFT method, assuming a slit pore geometry for the micropores based on the N_2 isotherm adsorption data. The PSD curves show that the most probable pore diameter (D_{NLDFT}) of AC-600 is 0.77 nm in contrast to 0.81 nm for AC-700 and 1.06 nm for AC-800 (Fig. 6b), indicating that the pores are enlarged by KOH etching under severe activation conditions. It is well know that KOH activation is an effective way to generate nano-scale pores in the final carbon materials. The KOH activation mechanism was suggested by Linares-Solano's group as follows [54], $6KOH + 2C \rightarrow 2K + 2K_2CO_3 + 3H_2$, followed by decomposition of K_2CO_3 and/or reaction of $K/K_2CO_3/CO_2$ with carbon.

To evaluate the electrochemical capacitive properties of the porous ACs as supercapacitor electrodes materials, cyclic voltammetry (CV) measurements were carried out in 6 M KOH aqueous electrolytes solution using three-electrode system. Fig. 7a depicts the CV curves of the porous ACs at a scan rate of 5 mV s^{-1}. The CV curves of all the samples display a rectangular-like shape with obvious hump at low potential region, and the hump becomes progressively less obvious with increased activation temperature due to the decreased amounts of active heteroatoms. It is also an indicative of the combination effects of electric double-layer capacitance (EDLC) and pseudo-capacitance (oxidation or reduction reaction) caused by the existence of active nitrogen and/or oxygen heteroatoms [8,51]. Among the samples tested, AC-600 exhibits the largest area of loop, suggesting the highest capacitance at low scan rate, which is consistent with the capacitance calculated by GCD curves. Fig. 7b shows the CV curves at high scan rate of 100 mV s^{-1}, as can be seen from the curves that AC-800 still presents better rectangular-like shape than AC-600 and AC-700. This might be due to its broader PSD and higher mesoporosity of AC-800 (as shown in Table 2) that benefit facile and fast electrolyte ion transport and shorten the diffusion distances from electrolyte to the inner micropore surface [24].

The capacitive performance of the porous ACs were further tested with galvanostatic charge-discharge (GCD) experiments at various current densities with the voltage windows the same as that of the CV analysis. The GCD curves are exhibited in Fig. 7c and Fig. S2. The specific capacitances of electrode materials are calculated from galvanostatic discharge curves by Eq. (1) and the results are listed in Table S1. It can be seen that all curves are almost symmetrical and linear at increased current densities ranging from 0.1 to 10 A g^{-1}, which is a typical characteristic of an ideal capacitor with good electrochemical reversibility. The inflections at ~−0.2 V of all samples imply the impact of pseudocapacitance due to the effect of active heteroatoms. Besides, AC-600 has shown great potential as electrode materials that is superior to most of the analogical carbon materials derived from other waste biomasses (as compared in Table 3). Although AC-600 has relatively low specific surface area (645 $m^2 g^{-1}$) than other carbon materials in the Table 3, its gravimetric specific capacitance (C_m) could reach to 279 F g^{-1}, while the surface specific capacitance (C_s) is about 43.3 μF cm^{-2} at close current density of 1 A g^{-1}. The high C_m of AC-600 may be due to the synergistic effect of the ultramicropores (<1 nm) and the rich active heteroatoms. In the KOH aqueous electrolytes solution, the micropores with pore size less than 0.5 nm are generally considered too narrow for double-layer formation and pores larger than 2 nm are too wide. Thus, the AC-600 that possesses concentrated pores size distribution of 0.77 nm is very suitable for the delivery of the electrolytes ions in the sample porous channels, and achieving high electrosorption efficiency, which also lead to improved specific capacitance [55]. Besides, the irreversible redox of the active heteroatoms induce extra pseudo-capacitance resulting in a high C_s [56]. Therefore, the better electrochemical performance of the AC-600 is induced by charging both the EDL and pseudofaradaic redox reactions involving the nitrogenated and/or oxygenated functionalities. Fig. 7d compares the capacitance retention of all samples at a range of current density from 0.1 to 10 A g^{-1}. At the current density of 0.1 A g^{-1}, the specific capacitance of 340, 309 and 253 F g^{-1} are obtained for AC-600, AC-700 and AC-800, respectively. At higher current density, the specific capacitance slightly decrease due to the sterical limitations of materials over which ions can only partially penetrate into the micropores [57,58]. However, at a current density of 10 A g^{-1}, AC-600 and AC-700 still maintain specific capacitances of 231 and 222 F g^{-1}, respectively. This is attributable to small amounts of mesoporous structure of the carbons that facilitate rapid electrolyte transfer and the

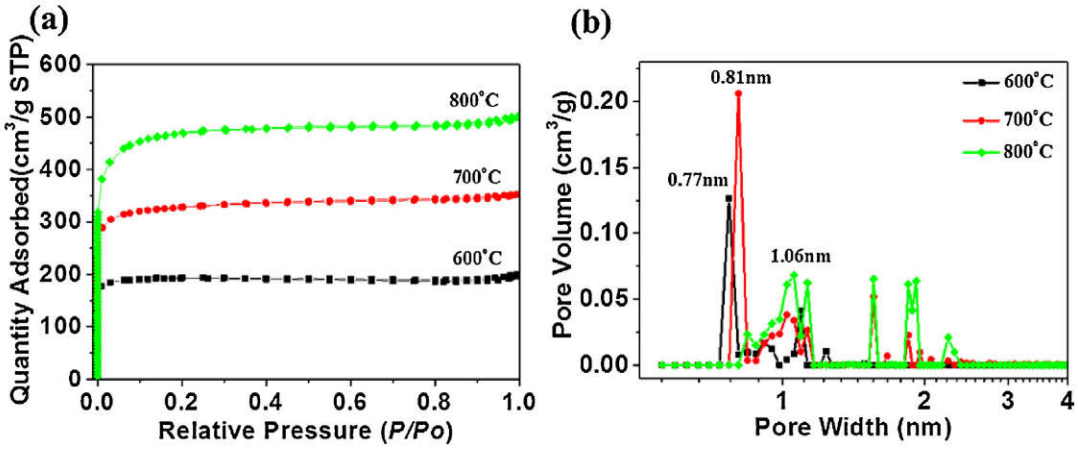

Fig. 6. (a) Nitrogen adsorption-desorption isotherms and (b) PSD curves of the porous ACs.

Table 2
The texture properties of the as-prepared ACs.

Sample	S_{BET} [$m^2 g^{-1}$][a]	S_{micro} [$m^2 g^{-1}$][b]	S_{meso} [$m^2 g^{-1}$][c]	V_{tot} [$cm^3 g^{-1}$][d]	V_{micro} [$cm^3 g^{-1}$][e]	D_{NLDFT} [nm][f]
AC-600	645	628	17	0.31	0.29	0.77
AC-700	1106	946	160	0.55	0.44	0.81
AC-800	1586	1296	290	0.78	0.60	1.06

[a] S_{BET} = apparent surface area calculated by the Brunauer–Emmett–Teller(BET) method.
[b] S_{micro} = micropore surface area calculated by t-plot method.
[c] S_{meso} = Substrct S_{micro} from S_{BET}.
[d] V_{tot} = total pore volume at P/P_0 = 0.99.
[e] V_{micro} = micropore volume calculated by t-plot method.
[f] D_{NLDFT} = the maximum value of the pore size distribution.

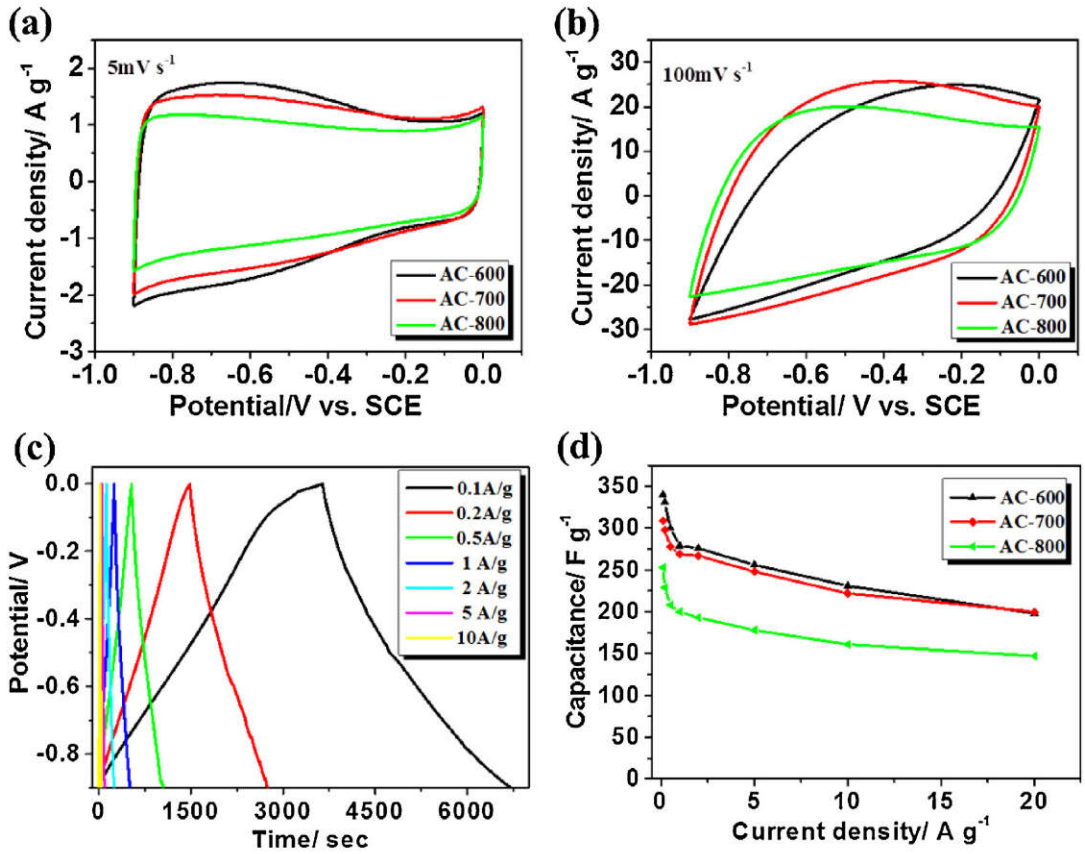

Fig. 7. CV curves of activated samples AC-600, AC-700 and AC-800 at scan rates of (a) 5 mV s^{-1}; (b) 100 mV s^{-1}; (c) GCD curves of AC-600 at different current densities (0.1-10 A g^{-1}); (d) the dependence of the capacitance of all samples as a function of current density.

relatively high degree of graphitization that imparts good electrical conductivity to the electrode. The results further demonstrate that despite moderate micropore surface area, appropriate PSD, rich active heteroatoms contents and good crystallinity make AC-600 have the best capacitive performance.

Fig. 8a shows the Nyquist plot of porous ACs in the frequency range from 100 kHz to 10 mHz under open circuit potential. The porous ACs display good capacitive behavior with nearly vertical slope at the low-frequency region. At very high frequency, the imaginary part (Z″) of the impedance is close to zero, while the real

Table 3
Comparison of the properties of carbon materials prepared from biomass wastes for supercapacitors in KOH aqueous electrolytes.

Materials	Activating agent	S_{BET} ($m^2 g^{-1}$)	C_m (F g^{-1})	C_s (μF cm^{-2})	Measurements condition	Electrolyte	Ref.
Corn grains	KOH	3199	257	8	1 mA cm^{-2}	6 M KOH	[19]
Sunflower seed shell	KOH	2509	311	12.4	0.25 A g^{-1}	30 wt% KOH	[20]
Waste news paper	KOH	416	180	43.3	2 mV s^{-1}	6 M KOH	[29]
Enteromorpha- prolifera	KOH	2283	295	12.9	0.5 A g^{-1}	30 wt% KOH	[27]
Coconut shell	Steam	1532	228	14.9	5 mV s^{-1}	6 M KOH	[23]
Tea leaves	KOH	2841	330	11.6	1 A g^{-1}	2 M KOH	[17]
Fermented rice	KOH	2106	219	10.4	15 A g^{-1}	6 M KOH	[28]
Coconut shell	$ZnCl_2$	1874	268	14.3	1 A g^{-1}	6 M KOH	[24]
Willow catkins	KOH	645	279	43.3	1 A g^{-1}	6 M KOH	Our work

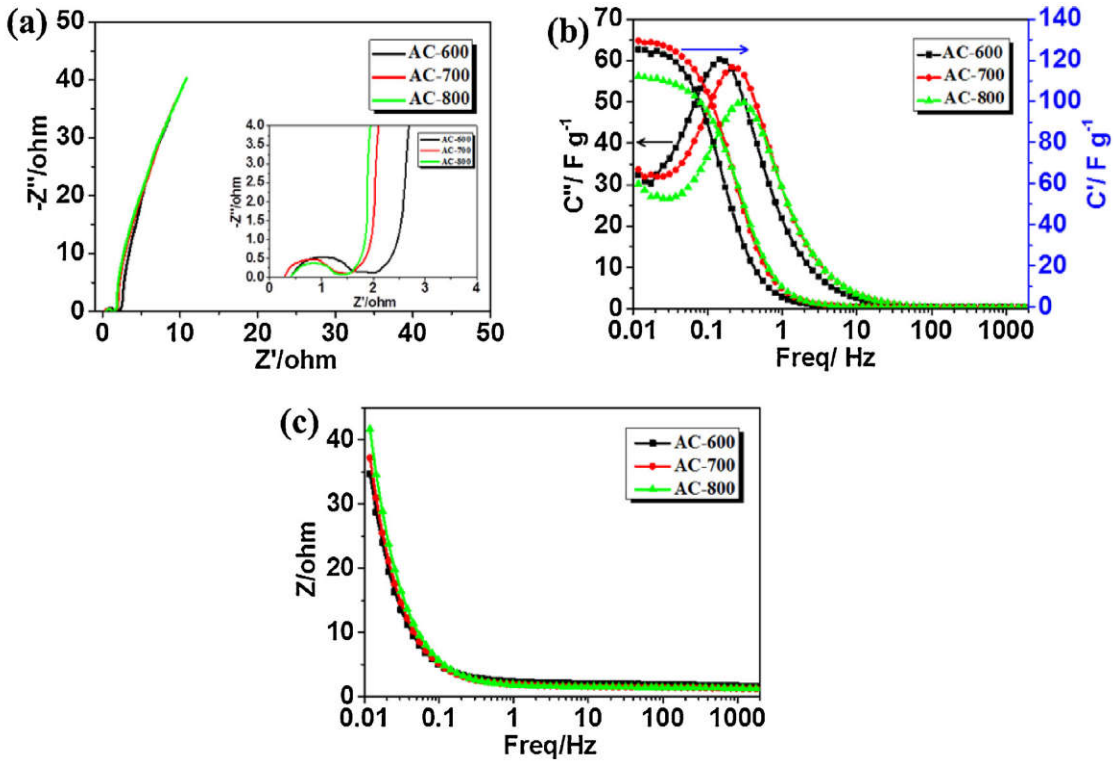

Fig. 8. (a) Nyquist plots of porous ACs, the inset shows the magnified view of the high-frequency region; (b) Frequency dependent real and imaginary capacitance plot; (c) Plot of total impedance versus frequency.

part of resistance (Z′) such as the intercept of plot with real axis, represents the equivalent series resistance (ESR) R_s which is a combination of the ionic resistance of the electrolyte, the intrinsic resistance of the activate materials and contact resistance with the current collector. The internal resistance of all samples are very low (below 0.5 Ω), indicating good conductivity of the test device in aqueous electrolytes. At medium–high frequencies, a distinct semicircle loop is observed, which stands for charge transfer resistance (R_{ct}) at the interface between electrolytes and electrode, as shown in the inset of the magnified high-frequency region of Fig. 8a. The small semicircle of the samples (nearly 1 Ω) indicates the good ionic conductivity owing to the high degree of graphitization that result in high electrical conductivity of electrode materials. The real capacitance (C′) and imaginary capacitance (C″) are calculated using Eqs. (6) and (7). The plots of frequency dependent real (C′) and imaginary (C″) capacitance are shown in Fig. 8b. In the low frequency region, the real capacitance (C′) remains a constant value which reflects the saturated capacitance at low frequency. The capacitance value decrease sharply at the frequency above 0.1 Hz and reach to constant above 10 Hz. At low frequency, electrolyte ions could penetrate inside the porous ACs and access to more electrode surface thereby contributing to high capacitance value. However, at high frequency, electrolyte ions can only access to the surface of carbon materials whereas the inner pores are not accessible that resulting in sharp decrease in the capacitance. The sharp peak in the frequency dependent imaginary capacitance (C″) plot shows the maximum capacitance at frequency of f_0 corresponding to the relaxation time as $\tau_0 = 1/f_0$ which are 5.8, 4.0 and 3.3 s for AC-600, AC-700 and AC-800, respectively. The relaxation time signifies the minimum time needed to discharge all the energy from the device with an efficiency of more than 50% [5]. The lowest relaxation time (~3.3 s) of AC-800 also indicates the greatest maximum accessibility of the electrolyte ions to the outer surface of the porous ACs among all the samples which is related to the larger pore size and broader PSD (Fig. 6b). The relationship between the total impedance and the frequency for the porous ACs are shown on Fig. 8c. When the frequency is low, the electrolyte ions try to penetrate from the orifice to the active materials pores. So the bottom of the pores will also devote to the resistive and the capacitive behavior that lead to higher impedance. However, at high frequency the electrolyte ions can only penetrate near the orifice of the pores. Hence, resistive and the capacitive behavior can only response near the orifice. The penetration degree decreases with the frequency increasing. At the frequency below 0.1 Hz, a straight line is obtained that is due to the accumulation of electrolyte ions at the bottom of pores. A horizontal line in the high frequency region signifies the dominance of electronic transport over this regime [59].

From electrochemical impedance spectroscopy measurements, it can be concluded that the electrode materials have low ionic resistance inside the porous structure that facilitate the fast diffusion of electrolyte ions into the porous network. Besides, the electrode materials have good conductivity and low charge transfer resistance that benefit fast charge transfer between the electrolytes and electrode materials. The results further demonstrate that the WCs derived ACs are promising electrode materials for supercapacitor applications.

The long-term cyclic stability is also a crucial factor for electrode materials in energy storage application. Fig. 9 shows the variation of capacitance retention and coulombic efficiency as a function of cycle number for AC-600 at a current density of 1 A g^{-1}. The specific capacitance decreases slowly at the first 250 cycles and maintains at about 92% of the initial specific capacitance with a slight fluctuation and the coulombic efficiency can retain nearly 100% over 3000 cycles, which indicates that the AC-600 electrode material displays good cyclic stability.

In a word, the AC-600 electrode material shows high specific capacitance and good rate capability and cycling stability because of the following structure and chemical composition properties:

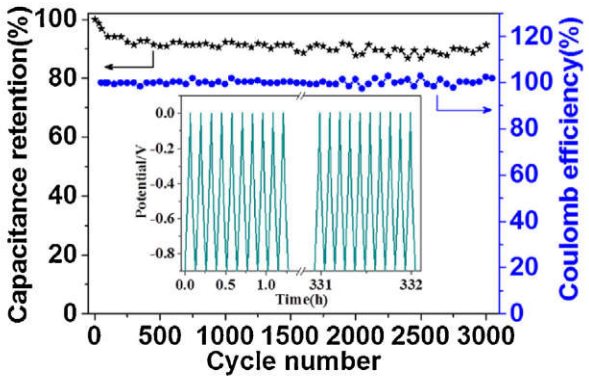

Fig. 9. Variation of the capacitance retention and Coulombic efficiency as a function of cycle number of AC-600 at a charge–discharge current density of 1 A g^{-1} in 6 M KOH electrolyte. Inset: galvanostatic charge–discharge cycles.

(1) moderate specific surface area but high effective micropore surface area that provide enough surface sites to form electrochemical double-layer; (2) the existence of rich surface active heteroatoms-doped functional groups, which not only improves the hydrophilicity and wettability of the porous ACs that results in good interfacial adhesion with electrolyte but also participates in reversible redox reaction and generates remarkable pseudocapacitance; (3) good electrical conductivity as well as high graphitizatin degree, which is also favorable to the high-performance capacitors.

4. Conclusions

In summary, sustainable and environmentally abundant WCs are employed as raw materials to prepare novel porous ACs by simple KOH-activation process for high performance supercapacitor electrodes. The AC products show unusual interconnected three-dimensional network structure composed of sheets-like primary particles. The higher activation temperature leads to the carbon materials with higher surface area and larger pore size, but lower surface heteroatoms-doped functional groups. The resultant carbon material activated at 600 °C possesses despite moderate specific surface area (645 $m^2 g^{-1}$), appropriate PSD (0.77 nm), rich surface heteroatoms-doped functional groups (2.51 wt.% N and 13.28 wt.% O species), high graphitization degree as well as good electrical conductivity, which results in excellent electrochemical properties due to the contribution of EDLCs and pseudo-capacitance. The specific capacitance of the porous ACs is 340 F g^{-1} at a current density of 0.1 A g^{-1} and 231 F g^{-1} even at 10 A g^{-1} with capacitance retention of 92% over 3000 cycles. This work presents a successful practice of preparing high value-added ACs from biomass WCs for energy storage applications.

Acknowledgments

This work was financially supported by the Natural Science Foundation of Shanxi Province (No. 2012011219-3) and Outstanding Young Talent Fund of Institute of Coal chemistry, Chinese Academy of Sciences.

Appendix A. Supplementary data

Supplementary data associated with this article can be found, in the online version, at http://dx.doi.org/10.1016/j.electacta.2015.03.048.

References

[1] L.L. Zhang, X.S. Zhao, Carbon-based materials as supercapacitor electrodes, Chem. Soc. Rev. 38 (2009) 2520.
[2] E. Raymundo-Piñero, M. Cadek, F. Béguin, Tuning Carbon Materials for Supercapacitors by Direct Pyrolysis of Seaweeds, Adv. Funct. Mater. 19 (2009) 1032.
[3] J. Yan, Q. Wang, T. Wei, Z. Fan, Recent Advances in Design and Fabrication of Electrochemical Supercapacitors with High Energy Densities, Adv. Energy Mater. 4 (2014) .
[4] P. Simon, Y. Gogotsi, Materials for electrochemical capacitors, Nat. Mater. 7 (2008) 845.
[5] D. Pech, M. Brunet, H. Durou, P. Huang, V. Mochalin, Y. Gogotsi, Ultrahigh-power micrometre-sized supercapacitors based on onion-like carbon, Nat. Nano 5 (2010) 651.
[6] H. Zhu, J. Yin, X. Wang, H. Wang, X. Yang, Microorganism-Derived Heteroatom-Doped Carbon Materials for Oxygen Reduction and Supercapacitors, Adv. Funct. Mater. 23 (2013) 1305.
[7] Z. Li, Z. Xu, X. Tan, H. Wang, C. Holt, T. Stephenson, Mesoporous nitrogen-rich carbons derived from protein for ultra-high capacity battery anodes and supercapacitors, Energy Environ. Sci. 6 (2013) 871.
[8] L.F. Chen, X.D. Zhang, H.W. Liang, M. Kong, Q.F. Guan, P. Chen, Synthesis of Nitrogen-Doped Porous Carbon Nanofibers as an Efficient Electrode Material for Supercapacitors, ACS Nano 6 (2012) 7092.
[9] A. Alabadi, X. Yang, Z. Dong, Z. Li, B. Tan, Nitrogen-doped activated carbons derived from a co-polymer for high supercapacitor performance, J. Mater. Chem. A 2 (2014) 11697.
[10] Y. Korenblit, M. Rose, E. Kockrick, L. Borchardt, A. Kvit, S. Kaskel, High-Rate Electrochemical Capacitors Based on Ordered Mesoporous Silicon Carbide-Derived Carbon, ACS Nano 4 (2010) 1337.
[11] J. Li, X. Wang, Q. Huang, S. Gamboa, P.J. Sebastian, Studies on preparation and performances of carbon aerogel electrodes for the application of supercapacitor, J. Power Sources 158 (2006) 784.
[12] H. An, Y. Wang, X. Wang, L. Zheng, X. Wang, L. Yi, Polypyrrole/carbon aerogel composite materials for supercapacitor, J. Power Sources 195 (2010) 6964.
[13] Y. Zhu, S. Murali, M.D. Stoller, K.J. Ganesh, W. Cai, P.J. Ferreira, Carbon-Based Supercapacitors Produced by Activation of Graphene, Science 332 (2011) 1537.
[14] M.M. Titirici, R.J. White, C. Falco, M. Sevilla, Black perspectives for a green future: hydrothermal carbons for environment protection and energy storage, Energy Environ. Sci. 5 (2012) 6796.
[15] J. Wang, S. Kaskel, KOH activation of carbon-based materials for energy storage, J. Mater. Chem. 22 (2012) 23710.
[16] R. Wang, P. Wang, X. Yan, J. Lang, C. Peng, Q. Xue, Promising Porous Carbon Derived from Celtuce Leaves with Outstanding Supercapacitance and CO2Capture Performance, ACS Appl. Mater. Interfaces 4 (2012) 5800.
[17] C. Peng, X. Yan, R. Wang, J. Lang, Y. Ou, Q. Xue, Promising activated carbons derived from waste tea-leaves and their application in high performance supercapacitors electrodes, Electrochim. Acta 87 (2013) 401.
[18] M. Biswal, A. Banerjee, M. Deo, S. Ogale, From dead leaves to high energy density supercapacitors, Energy Environ. Sci. 6 (2013) 1249.
[19] M.S. Balathanigaimani, W.G. Shim, M. Lee, C. Kim, J.W. Lee, H. Moon, Highly porous electrodes from novel corn grains-based activated carbons for electrical double layer capacitors, Electrochem. Commun. 10 (2008) 868.
[20] X. Li, W. Xing, S. Zhuo, J. Zhou, F. Li, S.Z. Qiao, Preparation of capacitor's electrode from sunflower seed shell, Bioresour. Technol. 102 (2011) 1118.
[21] F.C. Wu, R.L. Tseng, C.C. Hu, C.C. Wang, Effects of pore structure and electrolyte on the capacitive characteristics of steam- and KOH-activated carbons for supercapacitors, J. Power Sources 144 (2005) 302.
[22] F.C. Wu, R.L. Tseng, C.C. Hu, C.C. Wang, Physical and electrochemical characterization of activated carbons prepared from firwoods for supercapacitors, J. Power Sources 138 (2004) 351.
[23] J. Mi, X.R. Wang, R.J. Fan, W.H. Qu, W.C. Li, Coconut-Shell-Based Porous Carbons with a Tunable Micro/Mesopore Ratio for High-Performance Supercapacitors, Energy Fuels 26 (2012) 5321.
[24] L. Sun, C. Tian, M. Li, X. Meng, L. Wang, R. Wang, From coconut shell to porous graphene-like nanosheets for high-power supercapacitors, J. Mater. Chem. A 1 (2013) 6462.
[25] Y. Guo, J. Qi, Y. Jiang, S. Yang, Z. Wang, H. Xu, Performance of electrical double layer capacitors with porous carbons derived from rice husk, Mater. Chem. Phys. 80 (2003) 704–709.
[26] Y.J. Kim, B.J. Lee, H. Suezaki, T. Chino, Y. Abe, T. Yanagiura, Preparation and characterization of bamboo-based activated carbons as electrode materials for electric double layer capacitors, Carbon 44 (2006) 1592.
[27] X. Gao, W. Xing, J. Zhou, G. Wang, S. Zhuo, Z. Liu, Superior capacitive performance of active carbons derived from Enteromorpha prolifera, Electrochim. Acta 133 (2014) 459.
[28] S. Gao, Y. Chen, H. Fan, X. Wei, C. Hu, H. Luo, Large scale production of biomass-derived N-doped porous carbon spheres for oxygen reduction and supercapacitors, J. Mater. Chem. A 2 (2014) 3317.
[29] D. Kalpana, S.H. Cho, S.B. Lee, Y.S. Lee, R. Misra, N.G. Renganathan, Recycled waste paper—A new source of raw material for electric double-layer capacitors, J. Power Sources 190 (2009) 587.
[30] H. Zhu, X. Wang, F. Yang, X. Yang, Promising carbons for supercapacitors derived from fungi, Adv. Mater. 2 (2011) 2745.

[31] P.A. Goodman, H. Li, Y. Gao, Y.F. Lu, J.D. Stenger-Smith, J. Redepenning, Preparation and characterization of high surface area, high porosity carbon monoliths from pyrolyzed bovine bone and their performance as supercapacitor electrodes, Carbon 55 (2013) 291.
[32] W. Huang, H. Zhang, Y. Huang, W. Wang, S. Wei, Hierarchical porous carbon obtained from animal bone and evaluation in electric double-layer capacitors, Carbon 49 (2011) 838.
[33] Q. Wang, Q. Cao, X. Wang, B. Jing, H. Kuang, L. Zhou, A high-capacity carbon prepared from renewable chicken feather biopolymer for supercapacitors, J. Power Sources 225 (2013) 101.
[34] Y. Ma, J. Zhao, L. Zhang, Y. Zhao, Q. Fan, X. Li, The production of carbon microtubes by the carbonization of catkins and their use in the oxygen reduction reaction, Carbon 49 (2011) 5292.
[35] Z.G. Shi, T. Zhang, L.Y. Xu, Y.Q. Feng, A template method for the synthesis of hollow carbon fibers, Microporous Mesoporous Mater. 116 (2008) 698.
[36] C.Y. Wang, M.W. Li, Y.L. Wu, C.T. Guo, Preparation and microstructure of hollow mesophase pitch-based carbon fibers, Carbon 36 (1998) 1749.
[37] J.J.M. Orfão, F.J.A. Antunes, J.L. Figueiredo, Pyrolysis kinetics of lignocellulosic materials—three independent reactions model, Fuel 78 (1999) 349.
[38] A.J. Tsamba, W. Yang, W. Blasiak, Pyrolysis characteristics and global kinetics of coconut and cashew nut shells, Fuel Process. Technol. 87 (2006) 523.
[39] D. Vamvuka, E. Kakaras, E. Kastanaki, P. Grammelis, Pyrolysis characteristics and kinetics of biomass residuals mixtures with lignite, Fuel 82 (2003) 1949.
[40] T.H. Liou, Evolution of chemistry and morphology during the carbonization and combustion of rice husk, Carbon 42 (2004) 785.
[41] E. de Morais Teixeira, A. Corrêa, A. Manzoli, F. de Lima Leite, C. de Oliveira, L. Mattoso, Cellulose nanofibers from white and naturally colored cotton fibers, Cellulose 17 (2010) 595.
[42] A. Kaushik, M. Singh, G. Verma, Green nanocomposites based on thermoplastic starch and steam exploded cellulose nanofibrils from wheat straw, Carbohydr. Polym. 82 (2010) 337.
[43] L. Qie, W.M. Chen, Z.H. Wang, Q.G. Shao, X. Li, L.X. Yuan, Nitrogen-Doped Porous Carbon Nanofiber Webs as Anodes for Lithium Ion Batteries with a Superhigh Capacity and Rate Capability, Adv. Mater. 24 (2012) 2047.
[44] W. Qiao, S.H. Yoon, I. Mochida, KOH Activation of Needle Coke to Develop Activated Carbons for High-Performance EDLC, Energy Fuels 20 (2006) 1680.
[45] V. Zólyomi, J. Koltai, J. Kürti, Resonance Raman spectroscopy of graphite and graphene, physica status solidi (b) 248 (2011) 2435.
[46] W. Qian, F. Sun, Y. Xu, L. Qiu, C. Liu, S. Wang, Human hair-derived carbon flakes for electrochemical supercapacitors, Energy Environ. Sci. 7 (2014) 379.
[47] Y. Guo, D.A. Rockstraw, Activated carbons prepared from rice hull by one-step phosphoric acid activation, Microporous Mesoporous Mater. 100 (2007) 12.
[48] G.P. Hao, W.C. Li, D. Qian, A.H. Lu, Rapid Synthesis of Nitrogen-Doped Porous Carbon Monolith for CO_2 Capture, Adv. Mater. 22 (2010) 853.
[49] T.H. Liou, S.J. Wu, Characteristics of microporous/mesoporous carbons prepared from rice husk under base- and acid-treated conditions, J. Hazard. Mater. 171 (2009) 693.
[50] F. Su, C.K. Poh, J.S. Chen, G. Xu, D. Wang, Q. Li, Nitrogen-containing microporous carbon nanospheres with improved capacitive properties, Energy Environ. Sci. 4 (2011) 717.
[51] D. Hulicova-Jurcakova, M. Seredych, G.Q. Lu, T.J. Bandosz, Combined Effect of Nitrogen- and Oxygen-Containing Functional Groups of Microporous Activated Carbon on its Electrochemical Performance in Supercapacitors, Adv. Funct. Mater. 19 (2009) 438.
[52] C.O. Ania, V. Khomenko, E. Raymundo-Piñero, J.B. Parra, F. Béguin, The Large Electrochemical Capacitance of Microporous Doped Carbon Obtained by Using a Zeolite Template, Adv. Funct. Mater. 17 (2007) 1828.
[53] J. Yin, D. Zhang, J. Zhao, X. Wang, H. Zhu, C. Wang, Meso- and micro- porous composite carbons derived from humic acid for supercapacitors, Electrochim. Acta 136 (2014) 504.
[54] M.A. Lillo-Ródenas, D. Cazorla-Amorós, A. Linares-Solano, Understanding chemical reactions between carbons and NaOH and KOH: An insight into the chemical activation mechanism, Carbon 41 (2003) 267.
[55] E. Raymundo-Piñero, K. Kierzek, J. Machnikowski, F. Béguin, Relationship between the nanoporous texture of activated carbons and their capacitance properties in different electrolytes, Carbon 44 (2006) 2498.
[56] W. Si, J. Zhou, S. Zhang, S. Li, W. Xing, S. Zhuo, Tunable N-doped or dual N, S-doped activated hydrothermal carbons derived from human hair and glucose for supercapacitor applications, Electrochim. Acta 107 (2013) 397.
[57] A.G. Pandolfo, A.F. Hollenkamp, Carbon properties and their role in supercapacitors, J. Power Sources 157 (2006) 11.
[58] W. Xing, C.C. Huang, S.P. Zhuo, X. Yuan, G.Q. Wang, D. Hulicova-Jurcakova, Hierarchical porous carbons with high performance for supercapacitor electrodes, Carbon 47 (2009) 1715.
[59] J.G. Lee, J.Y. Kim, S.H. Kim, Effects of microporosity on the specific capacitance of polyacrylonitrile-based activated carbon fiber, J. Power Sources 160 (2006) 1495.